Boltzmann transport analysis for LMO

This document makes available the necessary information for this code to be useful. It includes the following parts:

1) Mathematical basis RTA model
2) Algorithmic implementation RTA model
3) Extension with *c*-axis warping
4) *c*-axis warping may be neglected.
5) Mathematical basis for the small-angle scattering (SAS) model
6) The algorithms used to evaluate the SAS model
7) Analytical proof that isotropic l_b gives rise to zero *b*-axis MR within RTA.
8) MR saturation

1) RTA model LMO

To compute the conductivity, we evaluate the following standard expression for the conductivity in a Boltzmann framework. Spin degeneracy is already included and Fermi surface broadening through thermal effects neglected.

$$\sigma_{ij} = \frac{e^2}{4\pi^3}\int_{FS} d^2k \frac{v_i}{\hbar v_F}\int_0^\infty dt\; v_j(-t)e^{-\frac{t}{\tau}} \qquad 1$$

Here, σ_{ij} is the conductivity with $i,j \in \{a,b,c\}$ the crystal directions, e the elementary charge quantum, FS denotes the Fermi surface sheet under consideration in *k*-space. Additional sheets add conductivities (parallel resistor). v_i is the velocity of the quasi-particle in direction i defined by $\hbar v_i \coloneqq \partial\epsilon/\partial k_i$ with $\epsilon(k)$ the dispersion, a subscript *F* denotes the Fermi velocity equivalent to $\sqrt{v_a^2 + v_b^2 + v_c^2}$. t is time and τ is the scattering lifetime.

Without c-axis warping one of the Fermi surface integrals directly yields $2\pi/c$.

$$\sigma_{ij} = \frac{e^2}{4\pi^2 c}\int_{FS} dk \frac{v_i}{\hbar v_F}\int_0^\infty dt\; v_j(-t)e^{-\frac{t}{\tau}} \qquad 2$$

The time integral will *not* be simplified further. We will algorithmically track cyclotron motion and keep the results accurate for general magnetic field to be able to study MR saturation. We also keep the time basis and do not transform to an $\omega_c t$-like basis for the latter struggles in the low-field limit where $\omega_c\tau \to 0$.

The last remaining integral is over the Fermi surface. Both in RTA and SAS models, we use k_a to parametrize the Fermi surface with limits $\pm\pi/a$. To do so, we use the following Jacobian that can be geometrically justified from the figure below. Alternatively, this can be derived purely analytically using $\hbar v_i \coloneqq d\epsilon/dk_i$. We also use symmetry to restrict ourselves to the positive-k_b sheet, to account for the other we add a factor 2.

$$dk = dk_a \frac{dk}{dk_a} = dk_a \frac{v_f}{v_b}$$

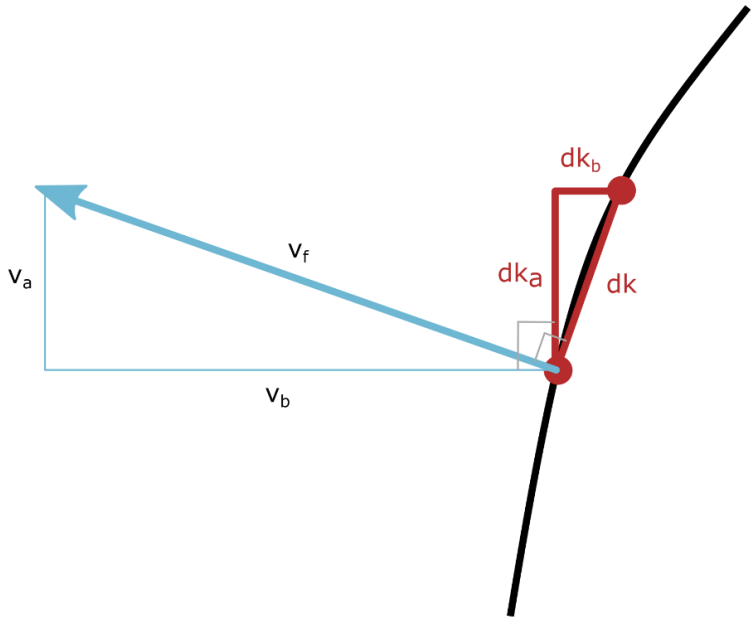

Which brings us to the final formula evaluated in the code. (Eq 1)

$$\sigma_{ij} = \frac{e^2}{2\pi^2 c\hbar} \int_{-\pi/a}^{\pi/a} dk_a \frac{v_i}{v_b} \int_0^\infty dt\, v_j(-t) e^{-\frac{t}{\tau}} \qquad 3$$

Time

We use isotropic τ, but to evaluate $v(-t)$ we nevertheless need to implement cyclotron motion. Following standard practise, we use Newton's equations on quasi-particles, which reads here with $\vec{B}$ along c:

$$\hbar \dot{k_a} = q v_b B \qquad 4$$

The velocity follows from the dispersion relation

$$\epsilon = -2t_a \cos(k_a a) - 2t_b \cos(k_b b)$$
$$\hbar \vec{v} = 2t_a a \sin(k_a a)\, \hat{a} + 2t_b \sin(k_b b)\, \hat{b} \qquad 5$$

We also check the total density contained in the Fermi surface using

$$n = \frac{1}{4\pi^3} \frac{2\pi}{c}\, area \qquad 6$$

Here, $area = 2\int_{-\pi/a}^{\pi/a} dk_a k_b$ is the area enclosed by the two sheets. The resistivity is evaluated with matrix inversion, e.g. $\rho_{bb} = \sigma_{aa}/(\sigma_{aa}\sigma_{bb} + \sigma_{ab}^2)$. This is only equal to $1/\sigma_{bb}$ when $\sigma_{ab} = 0$ (i.e. 0 T).

2) Algorithm RTA

We here mention in passing some of the key details of the algorithms used, but the implementation is ultimately in the code itself and the numerical methods are not fully explained.

First, we use the fact that the dispersion for a given k_a is monotonic in k_b. As a result, we can use binary search to quickly converge to the position of the Fermi surface for any given k_a value. This enables computationally cheap access to an arbitrary point on the Fermi surface.

Second, we use the fact that the RTA is only evaluated with isotropic τ such that $\exp\left(-\frac{t}{\tau}\right)$ is directly available at any time t. The code will cut off the time integral at a multitude of τ. This typically introduces an underestimate of the conductivity by a fraction $\exp\left(-\frac{t}{\tau}\right)$, which is treated as an error and kept small enough (typically $\ll 1e-10$). Extensions beyond isotropic τ are common, in particular isotropic l, but not the focus of this work.

Third, we evolve the quasi-particle position with cyclotron motion using Runge-Kutta 4 and Eq 1. Note that if one were to move beyond isotropic τ, the survival probability $\exp\left(-\frac{t}{\tau}\right)$ would also be evolved with time within this *same* RK4 step.

Fourth, we evaluate the time and k_a integral manually using Simpson's rule. This requires an odd number of points in time following the standard algorithm. For the k_a integral, we note that $\pm\pi/A$ are the same point translated by the Brillouin zone vectors. As a result, the weights are not 1,4,2,…,4,1 but we merge the first and final point to obtain 2,4,2,4,…,4 with an even number of points.

Fifth, we check the code against Drude theory in the zero-field limit to capture remaining any mistakes. We also test against expectation values for a full sheet traversal by cyclotron motion. Additionally, there are various smaller scale tests implemented in 'tests.py'.

3) *c*-axis warping

In the paper we state that *c*-axis warping is neglected. We do in fact do our due diligence and evaluate it to quantify this assumption.

It turns out this can be done simply if we restrict ourselves to $\rho_{aa}, \rho_{bb}, \rho_{ab}$. The integral to be evaluated follows from Eq. 1:

$$\sigma_{ij} = \frac{e^2}{4\pi^3}\int_{-\pi/c}^{\pi/c} dk_c \int_{-\pi/a}^{\pi/a} dk_a \frac{v_i}{\hbar v_b}\int_0^{\infty} dt\, v_j(-t)e^{-\frac{t}{\tau}} \quad 7$$

Note that other than the *c*-axis integral the entire formula is the same as before. Zooming in further, the dispersion also has nice properties:

$$\begin{aligned}\epsilon &= -2t_a\cos(k_a a) - 2t_b\cos(k_b b) - 2t_c\cos(k_c c)\\ \hbar\vec{v} &= 2t_a a\sin(k_a a)\,\hat{a} + 2t_b\sin(k_b b)\,\hat{b} + 2t_c\sin(k_c c)\,\hat{c}\end{aligned} \quad 8$$

The important point is there are no mixed terms. We can simply subtract the t_c term from the energy and ignore the $\hat{c}$ component of the velocity altogether. Ultimately, we arrive at the following formula to evaluate:

$$\sigma_{ij,warped} = \frac{c}{2\pi}\int_{-\pi}^{\pi} dk_c \sigma_{ij,unwarped}\,(\mu - 2t_c\cos(k_c c)) \quad 9$$

This only works for the components $\sigma_{aa}, \sigma_{bb}, \sigma_{ab}$. Throughout, we are assuming a quasi-1D Fermi surface. If we were to compute σ_{cc}, the *c*-axis component of the velocity must be considered. Note that $\sigma_{ac} = \sigma_{bc} = \sigma_{ca} = \sigma_{cb} = 0$ because the field is along the *c*-axis. This latter observation enables us to ignore *c*-axis components altogether to compute the ab resistivity, e.g. $\rho_{bb} = \sigma_{aa}/(\sigma_{aa}\sigma_{bb} + \sigma_{ab}^2)$.

The situation can be calculated using 'c_axis_calculate.py', and the results visualised with 'c_axis_visualize_results.py'. The results are also given below in figures. To account for the anisotropy $80:1:1600$ for $\rho_{aa}:\rho_{bb}:\rho_{cc}$ from [1] we estimate $\frac{\rho_{aa}}{\rho_{cc}} = \left(\frac{t_a a}{t_c c}\right)^2$ to obtain $t_c = t_a/3.3$.

4) *c*-axis warping may be neglected

The central conclusion is that c-axis warping may indeed be neglected given that we are looking for around 4 orders of magnitude change. Instead, for the Merino Fermi surface, the b-axis MR changes by around 3 % and the a-axis MR by less than 0.1 % at 100 T, see below. The resistivity ratio ρ_{aa}/ρ_{bb} is even less affected (0.02 %) than the a-axis MR. The latter observation justifies the use of $\frac{\rho_{aa}}{\rho_{cc}} = \left(\frac{t_a a}{t_c c}\right)^2$ to estimate the c-axis warping without changing t_a.

We also point out that the MR anisotropy ratio changed from 50115 without c-axis warping to 48551 with c-axis warping. The simple estimate from [2] used to estimate the MR anisotropy before these detailed models were developed yields 48808, in excellent agreement.

If we use the Nuss Fermi surface instead, the *b*-axis MR is increased by about 15%, the *a*-axis again by less than 0.1 % and the resistivity ratio is unaffected. The MR anisotropy ratio changes from 2.89e6 to 2.45e6 with the formula from Ref. [2] estimating 0.98e6. The factor 2 discrepancy from the estimate comes from the fact that the Nuss Fermi surface has two sheets with considerable difference in warping.

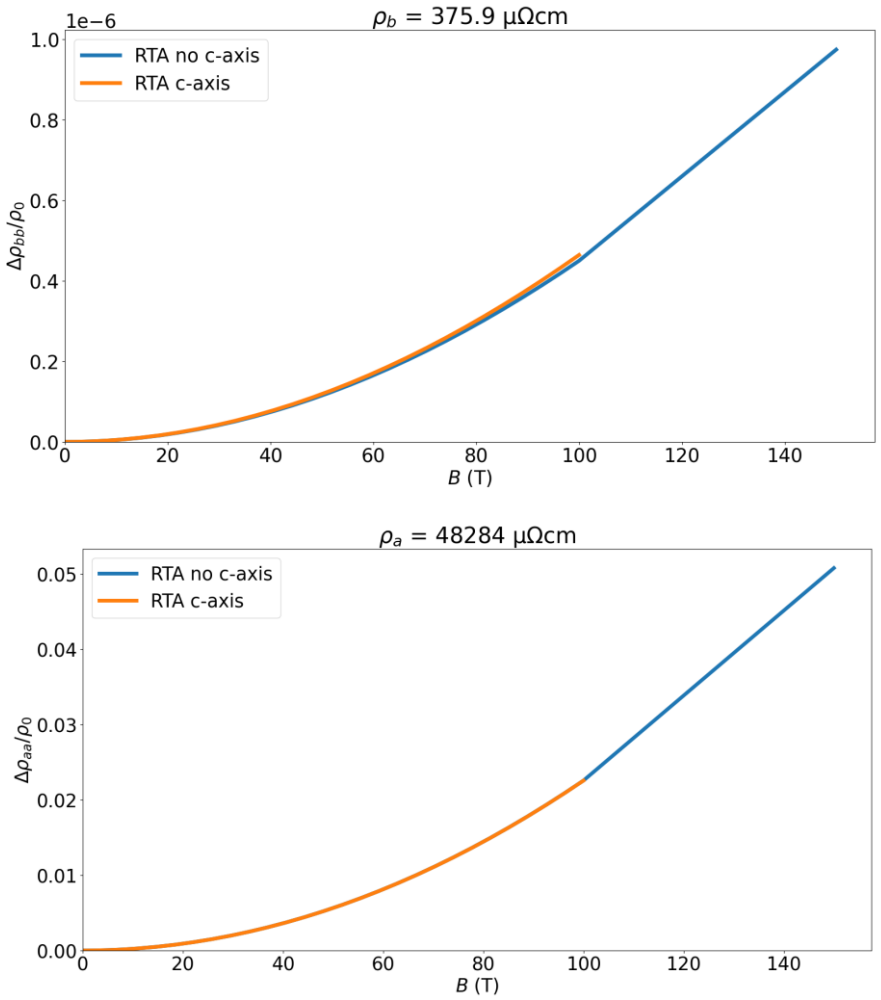

F1

Above is the Merino Fermi surface result with and without *c*-axis warping. We use for these calculations $\tau = 1e-14$ to obtain $l{\sim}1$ nm as given in the paper. This results in a zero-field resistivity in good agreement with the temperature sweeps shown in the supplement of the paper at 300 K.

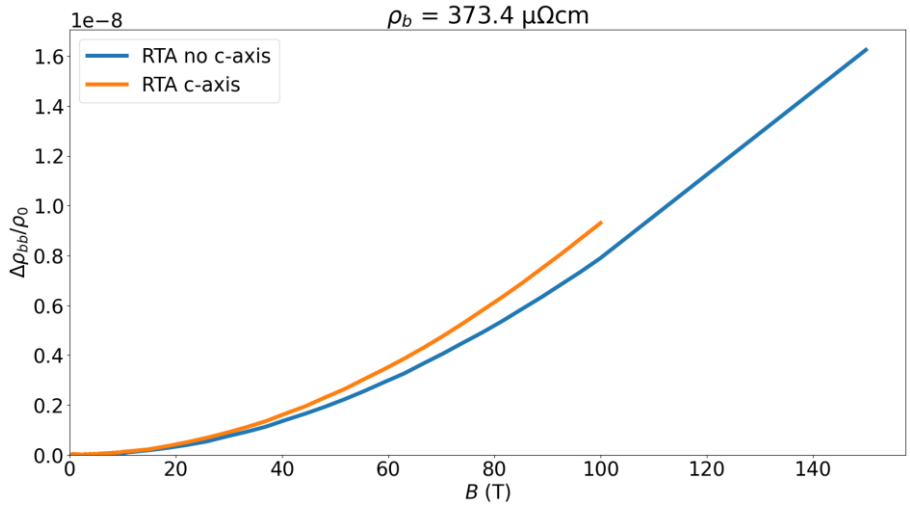

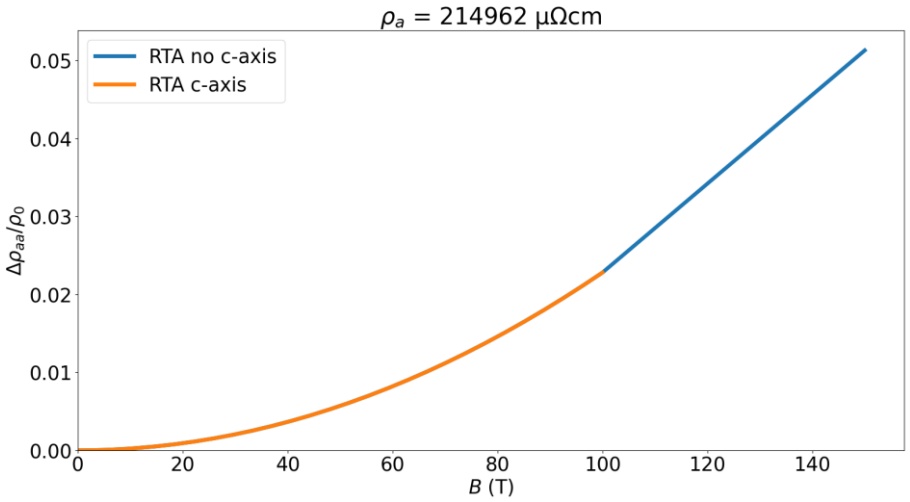

F2

The effect is somewhat larger on the Nuss Fermi surface, but still negligible to the 4-5 orders of magnitude required to explain the experimental *b*-axis MR. These results are generated with 'c_axis_calculate.py' and the graphs and statistics derived with 'c_axis_vizualize_results.py'.

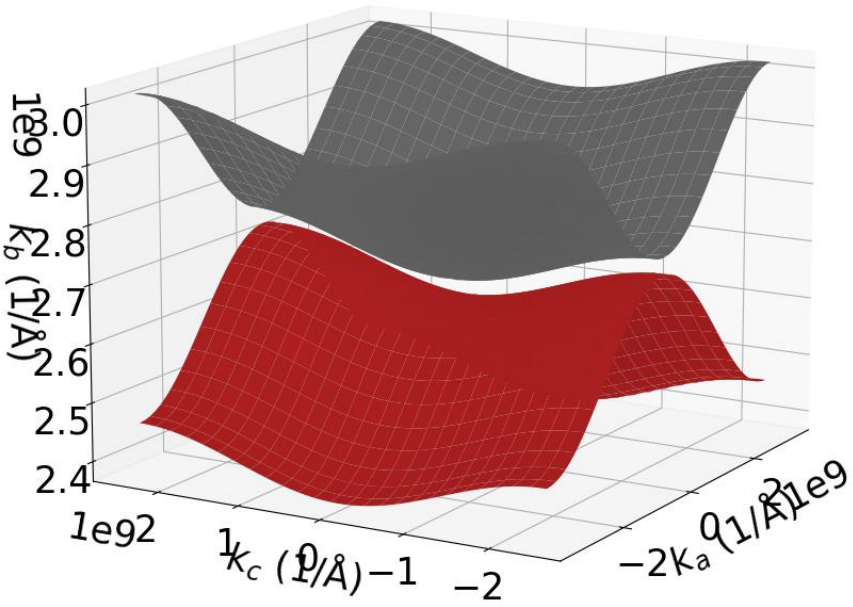

F3

This is a visualisation of the Merino Fermi surface using 'c_axis_warping_show.py'. Execute the code for an interactive version. Note that this only shows the positive-k_b sheet for clarity.

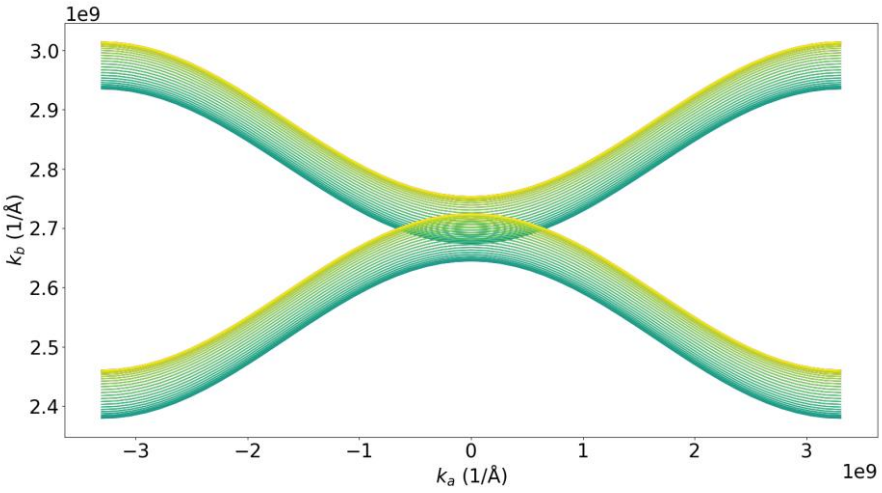

F4

This figure shows the warping for various k_c values. Notice that the sheets shift up and down, but the width is barely changing. This is because the dispersion is approximately linear in k_b near half filling, which means in leading order the c-axis dispersion leaves the Fermi surface corrugation unaffected and merely shifts it along k_b. The same holds for the velocity, which is why the influence of t_c is even less than expected from its size relative to t_a.

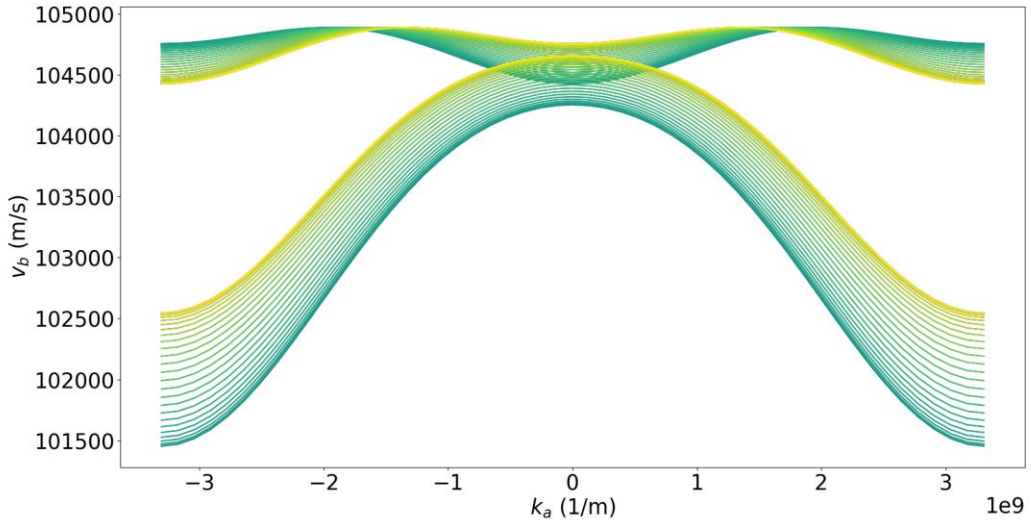

F4

Above: Variation of v_b introduced by the c-axis warping. Each curve represents a different k_c value and both Fermi pockets are shown. Although t_c is about 2.4 % of t_b, the velocity on the sheet closest to half filling is varying by an order of magnitude less. The sheet further away from half filling already had 1 % variation of v_b because of t_a. This pattern is shifting up and down with k_c and not changing much. As a result, these effects average out almost entirely for the zero-field resistivity.

5) SAS model maths

The small angle scattering model is beyond the relaxation time approximation. Instead of the RTA formula (Eq. 3):

$$\sigma_{ij} = \frac{e^2}{2\pi^2 c\hbar}\int_{-\pi/a}^{\pi/a} dk_a \frac{v_i}{v_b}\int_0^{\infty} dt\; v_j(-t)e^{-\frac{t}{\tau}}$$

We now use

$$\sigma_{ij} = \frac{e^2}{2\pi^2 c\hbar}\int_{-\pi/a}^{\pi/a} dk_a \frac{v_i}{v_b}\int_0^{\infty} dt \sum_{m=sheets}\int_{-\pi/a}^{\pi/a} dk'_a v_{j,k}(-t)u_m(k'_a,-t) \qquad 10$$

Here, we introduce u. At any given time t, $u_m(k_a)$ is the statistical weight / probability of the quasiparticle to be at any given point on the Fermi surface on sheet $m \in \{1,2\}$. This includes the second sheet at negative k_b. At all times, we maintain

$$1 = \sum_{m=sheets}\int_{-\pi/a}^{\pi/a} dk_a\, u_m(k_a,t) \qquad 11$$

Unlike the relaxation time approximation where an effective scattering time τ is taken over which the velocity correlation dissipates, we now always maintain charge conservation. This is the key characteristic that makes the SAS model more realistic.

u starts off at time 0 as a delta function at k_a on the positive sheet (the outermost integral), i.e. $u(k'_a,0) = \delta(k_a - k'_a)$. Relaxation of the velocity arises from washing out of *u* under scattering processes. The RTA is recovered if we take $u(k'_a,t) = \delta(k_a(t) - k'_a)\exp\left(-\frac{t}{\tau}\right)$, i.e. a moving delta function which exponentially loses charge over time. With SAS, u does not decay but approaches a symmetric distribution similar to the density of states in which $< v >= 0$.

Scattering events with an isotropic final state in k immediately lead to $< v(t) > = 0$ after the scattering and can be effectively captured by the relaxation time approximation. In SAS, phase coherence is broken but the velocity is barely relaxed. To test if SAS may explain any of the observed MR, we here implement the extreme limit of SAS. This limit was worked out by Pippard [3] and comes down to a diffusion equation on *u*.

$$\frac{du}{dt} = D\nabla_{\mathrm{k}}^2 u + \left.\frac{\partial u}{dt}\right|_{cycl} + \left.\frac{\partial u}{dt}\right|_{back} \qquad 12$$

Alongside diffusion we need cyclotron motion using Newton's equation to drive any MR:

$$\left.\frac{\partial u}{\partial t}\right|_{cycl} = \overrightarrow{\nabla_k} u \cdot \frac{\partial \vec{k}}{\partial t} = \overrightarrow{\nabla_k} u \cdot \frac{q\vec{v}\times\vec{B}}{\hbar} \qquad 13$$

Finally, we need backscattering. The reason is that $< v_b > \sim 1e5$ m/s averaged over a sheet, which is not zero. Hence, even if diffusion can homogenize u across the sheet, there will be a net v_b at late times. This means the conductivity is infinite. To relax v_b, we need an inter-sheet scattering mechanism. We choose here to model this with backscattering, i.e. $k_b \to -k_b$ while preserving k_a. This is inspired by *real* space scattering events on an impurity or exciton pair as the physical origin and also the reason that we initially seek to implement isotropic l_b. We will see later that this leads to zero MR and we are thus forced to also implement isotropic τ_{bs}.

The net scattering is proportional to the difference in occupation between the two states involved. To let the diffusion constant D be constant over the Fermi surface, but work in a k_a basis, we obtain the following Jacobian, which can be derived similar as in section 1.

$$\frac{du_m}{dt} = \frac{D}{1 + v_a^2/v_b^2}\frac{\partial^2 u_m}{\partial k_a^2} + \frac{e}{\hbar} v_b B \frac{\partial u_m}{\partial k_a} + P(u_{2-m} - u_m) \qquad 14$$

Each of the above terms can be visualised in isolation. The code for these visualisations is in the tests, set their respective "show = True" to get these graphs.

Processes

An example of diffusion. Note that $t = 0$ is a δ function where the 1 fs distribution is maximum. The black line separates the positive-k_b sheet (left) from the negative-k_b sheet. Diffusion has no interaction between the sheets. The lifetime is 10 fs.

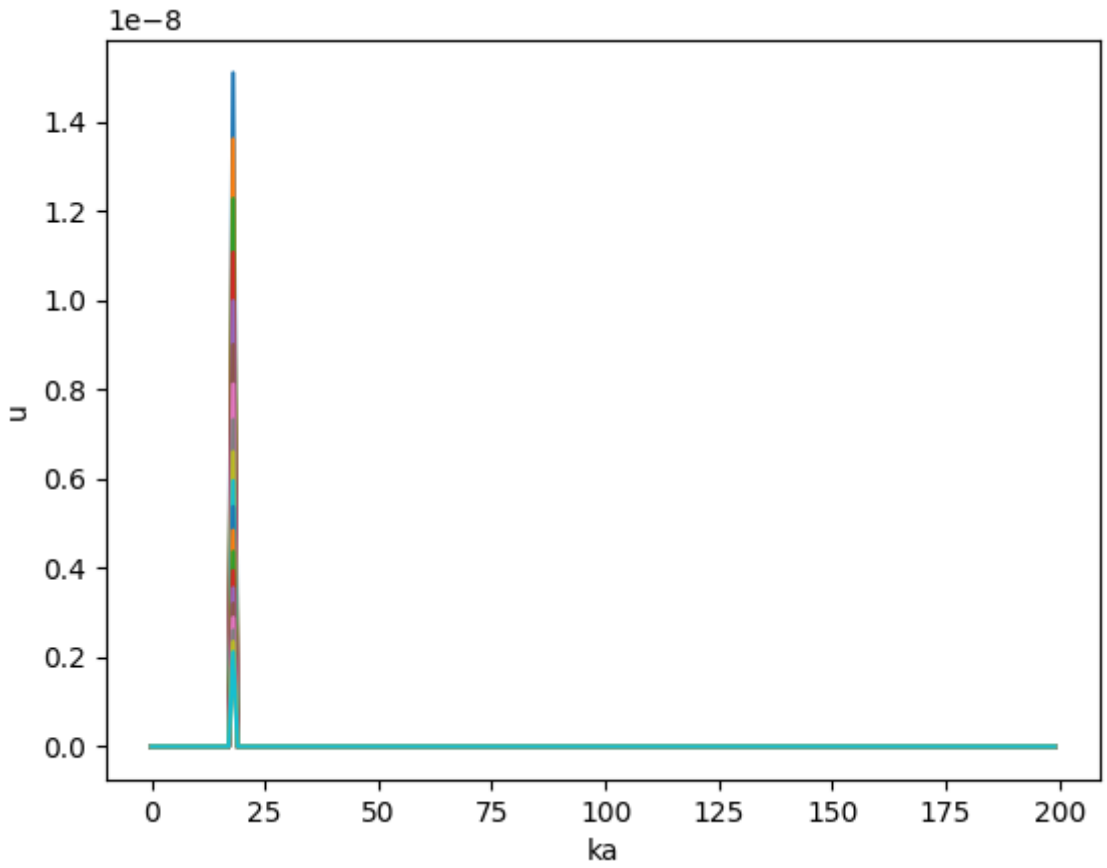

Bs_type=5, this is the only mode that violates charge conservation. This is an imitation of RTA with direct exponential decay of the state. (there are 100 points per FS sheet here).

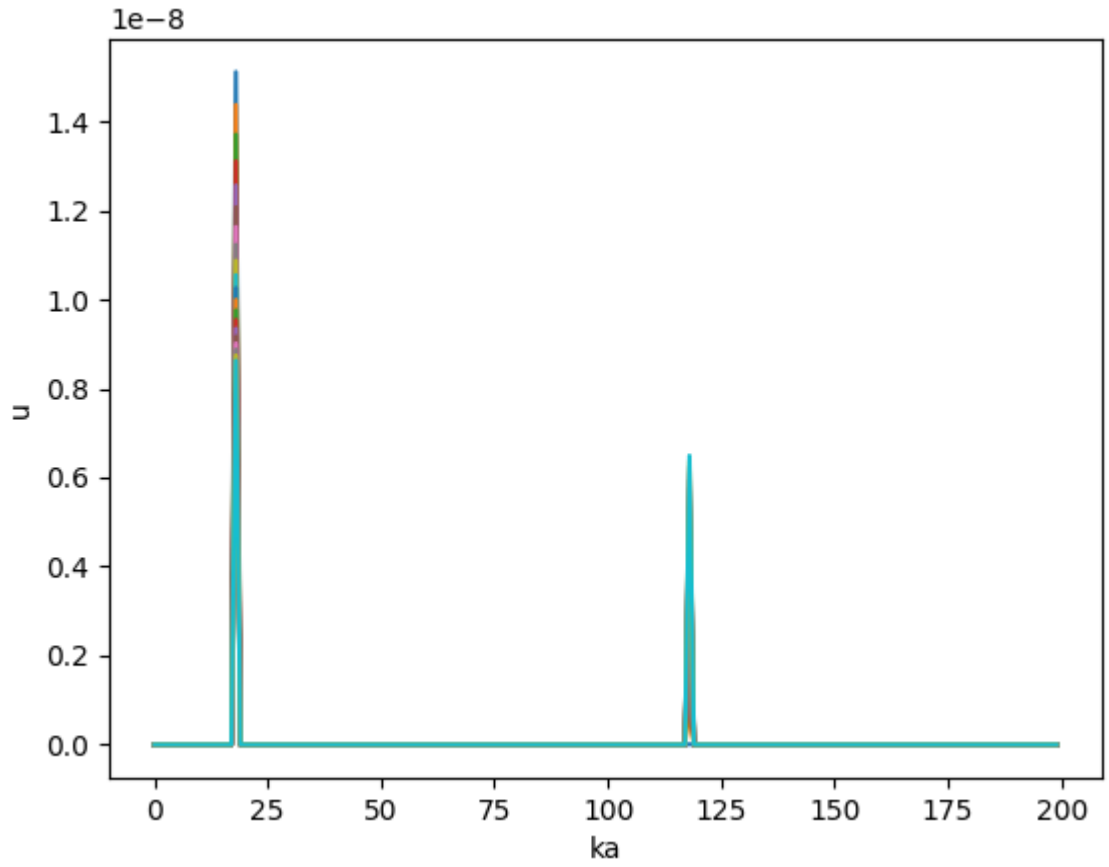

Backscattering (bs_type=1 or 2) equilibrates weights on the two sheets (separated at ka index 100) at the same ka value but opposite k_b. This is effectively exponential decay.

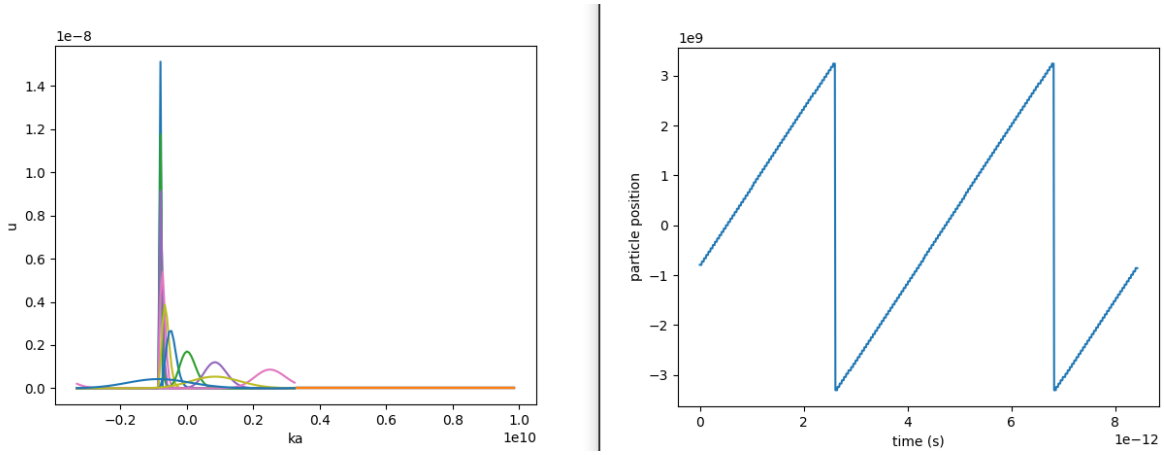

Cyclotron motion. It may be seen that some broadening occurs even without scattering rate. This is a numerical aberration unfortunately and at the root of the small difference in MR saturation in RTA and beyond RTA in the 'tests' section below. Essentially, because cyclotron motion is based on weight transfer between fixed k points, there is an essential broadening involved. But moving the underlying k basis requires re-creating M every time step, which is computationally unfeasible. Something that can be innovated upon, but which does not change the results noticeably (as proven by the RTA correspondence). The Brillouin zone time extracted by following the maximum matches the classical expectation.

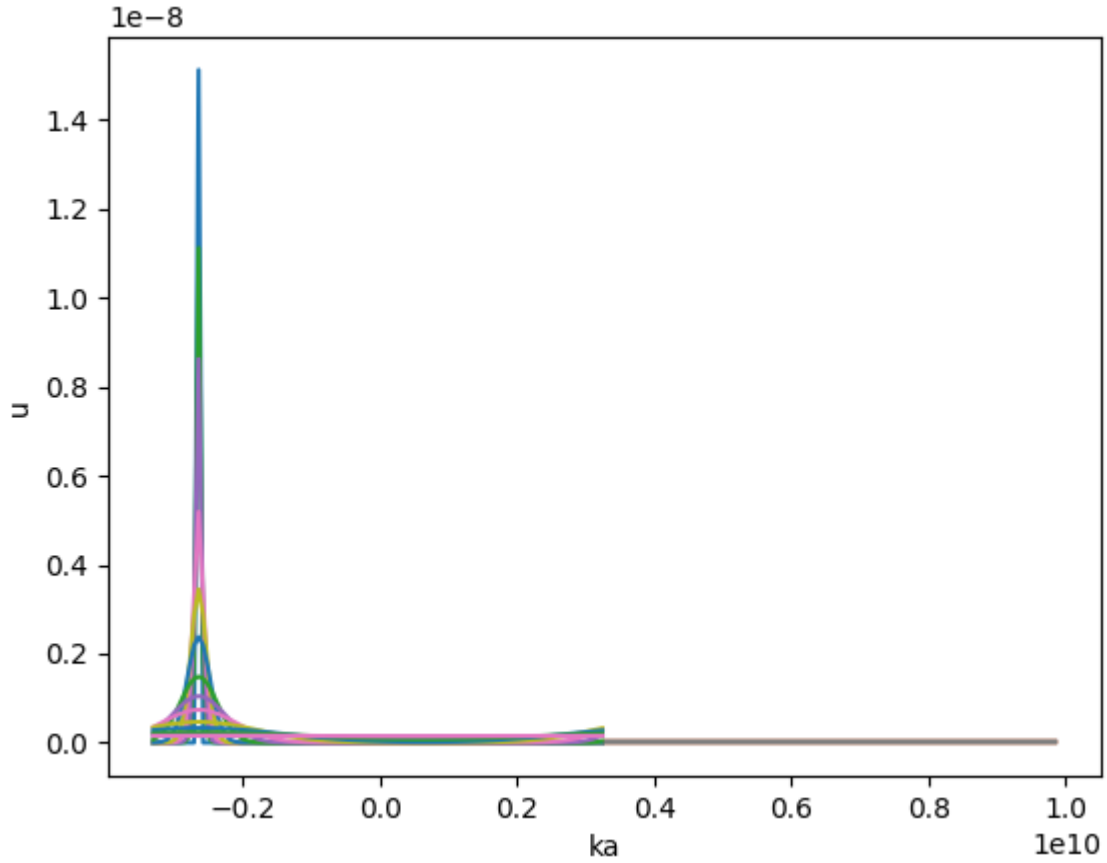

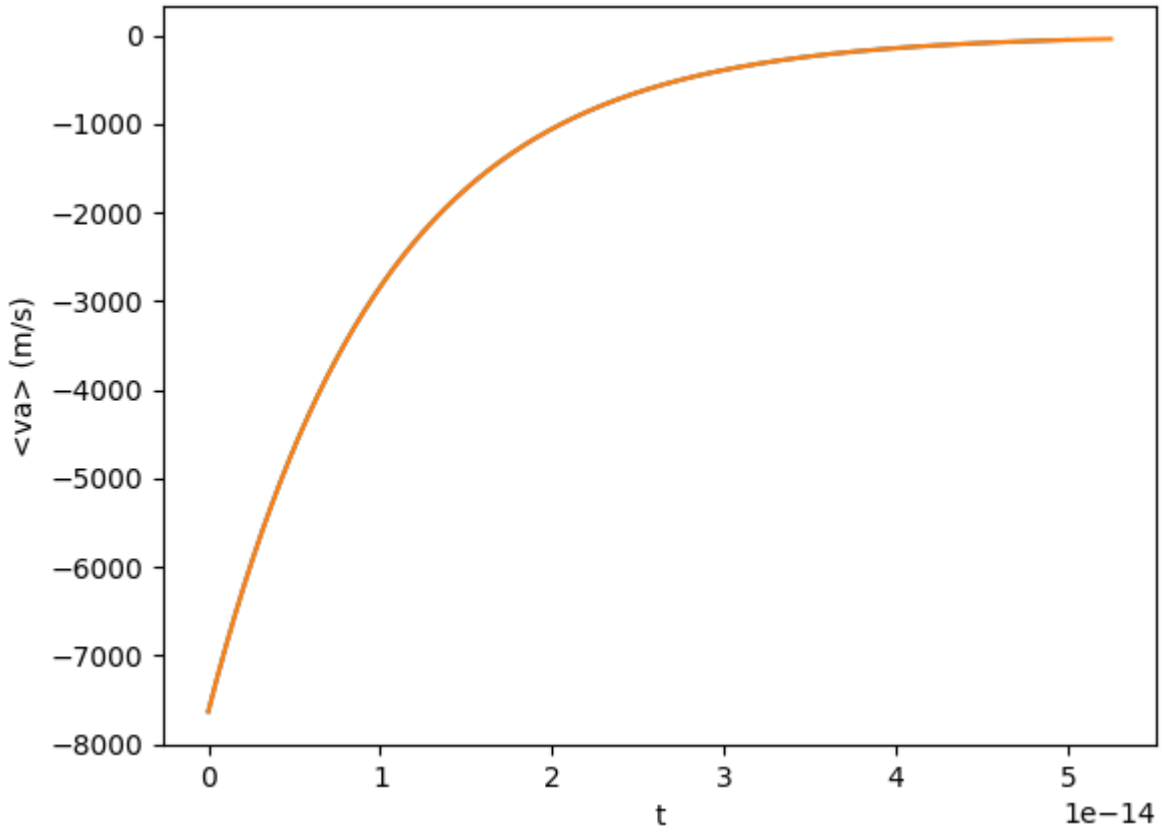

Diffusion and the effective relaxation time behaviour $\exp\left(-\frac{t}{\tau}\right)$ of v_a under small angle scattering.

6) Algorithm for SAS model

The algorithm used for the SAS model is considerably more complicated than the RTA model. There are minor reasons for this such as the extra integral, but the principal reason is the complicated time evolution in this model compared to an isotropic-τ RTA model. Combined with the requirement of high precision to compute small b-axis MR down to 1e-10, we need to use an efficient algorithm that also converges fully as the calculation becomes more accurate.

In the spirit of a data first approach, the code uses a $\vec{u}$ which is $2n$ in length which runs from $-\pi/a$ to π/a over the positive-k_b branch and then from $-\pi/a$ to π/a over the negative-k_b branch. Here, n are the number of points on a single Fermi sheet, the published results mostly use 512 and otherwise 1024. Make_state() initialises $\vec{u}(t=0)$ with a δ-function in this discretised k-space.

Separability and cyclotron motion

The first task to perform on this data is time evolution and for that, k differentiation over discrete Δk is required. The key aspect to realise here is that k and t are separable. Let $u = K(k)T(t)$ then Eq. 14 can be written as

$$\frac{1}{T}\frac{\partial T}{\partial t} = \frac{D}{1+v_a^2/v_b^2}\frac{1}{K}\frac{\partial^2 K}{\partial k^2} + \frac{e}{\hbar}\frac{v_b B}{K}\frac{\partial K}{\partial k} + \frac{P(K(-k_b)-K)}{K}$$

Note that v, D and P may have k-dependence but no time dependence. Just like in classical mechanics, we can now vary time on the left-hand side and realise the right-hand side is constant. Similarly, vary k on the right-hand side but the left-hand side is unchanging.

Why is this realisation important? It shows that we are allowed to quantise the t and k behaviour *independently* since *T* and *K* are independent in the face of derivatives. Focus on k first. Consider Runge Kutta 4 for the 1st order k-derivative that appears for cyclotron motion:

$$f = \frac{\partial u}{\partial k}$$
$$k_1 = f(k,t) = ev_b B/\hbar$$
$$k_2 = f\left(k+\frac{1}{2}\Delta k, t+\frac{1}{2}k_1\Delta k\right)$$
$$k_3 = f(k+\frac{1}{2}\Delta k, t+\frac{1}{2}k_2\Delta k)$$
$$k_4 = f(k+\Delta k, t+\frac{1}{2}k_3\Delta k)$$
$$u(k+\Delta k) \approx \frac{\Delta k}{6}(k_1+2k_2+2k_3+k_4)$$

The advantage that comes from the above observation is that f does *not* depend on time.

$$k_1 = f(k) = ev_b(k)Bu/\hbar$$
$$k_2 = f\left(k+\frac{1}{2}\Delta k\right)$$
$$k_3 = f(k+\frac{1}{2}\Delta k)$$
$$k_4 = f(k+\Delta k)$$

By evaluating a single point precisely halfway in between k and $k + \Delta k$ (the next point in the u matrix) we can therefore use RK4 to discretise the differential equation for cyclotron motion. We require the use of upwind differencing, which is to say that we do this between u^j and u^{j+1} if cyclotron motion pushes weight to increasing k_a and between u^j and u^{j-1} otherwise. This is necessary because otherwise u will develop negative elements, and this violates the formal treatment of u as a statistical distribution. See W. H. Press - Numerical Recipes ch19.1 for details. This situation arises because of the necessary discontinuity (non-smoothness) in u at $t = 0$. To ensure this never happens by mistake, the code asserts that $\min(u) \geq 0$ at every time step, always.

Notice also that the differential $\partial u/\partial k$ is here implemented as a net transfer of statistical weight. This is mathematically equivalent, but computationally fundamentally different from the RTA. Whereas in RTA we effectively keep the distribution and shift the underlying k value, here the k values are static and the weight is transferred between those fixed points.

Diffusion and back-scattering

Diffusion is second order and cannot use RK4, we instead use the standard lowest-order form

$$\frac{\partial^2 u}{\partial k_a^2} \to \frac{u^{j+1} - 2u^j + u^{j-1}}{(\Delta k_a)^2}$$

For backscattering, we can evaluate the difference directly. Notice that the lowest order convergence introduced by the discretisation of the differentials is therefore in the diffusion term and thus relaxation of v_a.

The state integral k_a' is evaluated using trapezoidal rule with the first and last point on each sheet merged such that every point has equal weight. Simpson's rule could not be used because the above algorithm assumes equivalence of all u locations and Simpson's does not. This is normally not an issue, but the state in question is discontinuous at $t = 0$ and that is why we cannot use a faster converging algorithm. Because of the diffusion term and trapezoidal rule, we ultimately need a lot more nr_ka for k_a' than time steps or k_a values.

Next, observe that *all* terms are linear in u, even after using RK4 the result is still linear in keeping with separability. All these terms can be summarised into a matrix, a differentiation operator which calculates the discrete-*k* and instantaneous-*t* evolution of the system.

$$\frac{\partial \vec{u}}{\partial t} = \widehat{M}\vec{u}$$

t-integral

This matrix $\widehat{M}$ is constructed such that the sum of every *column* is 0. That is to say, if a state such as $(0, 1, 0, \dots, 0)$ is the starting point, then $\partial\vec{u}/\partial t$ only redistributes charge and cannot create or destroy charge. It is possible to formulate the above arguments with rows summing to 0 instead, but in this case charge conservation is not satisfied. This happened in an earlier implementation and the result is errors scaling as $O\left(\frac{1}{n}\right)$, but the number of errors is $O(n)$ and so we end up with systematic errors. These tended to be of order 1e-4, which is sufficient to overwhelm any MR along the b-axis and can easily be mistaken for a true result. To avoid any such errors, we perform a detailed comparison with RTA below.

We now move to the next integral, which is time. RK4 is only useable on 1st order derivatives as we discovered for diffusion, but there is no issue with matrix equations. To evolve time, we construct a new matrix R with discrete *k* and *t* as follows:

$$k_1 = M$$

$$k_2 = \hat{I} + \frac{1}{2} dt \widehat{M}$$

$$k_3 = \hat{I} + \frac{1}{2} dt \widehat{k_2}$$

$$k_4 = \hat{I} + dt\, \widehat{k_3}$$

$$R = \frac{dt}{6}(k_1 + 2k_2 + 2k_3 + k_4)$$

Note that the power of this algorithm is resting on the fact that M is only generated once and unchanging. Variation over k is encoded and variation over t is absent from (again) separability. In other words, although u changes in k over time, the coefficients of M remain unchanged. Without this separability, time and k could not be separated and a different (more costly) algorithm found.

To further optimize the algorithm, we eliminate one more inefficiency. As shown below, the contribution to σ falls off exponentially over time even beyond the RTA - which is part of the unreasonable effectiveness of the RTA. Thus, early times require a smaller timestep than later times. To give an idea, we typically integrate up to 30 times the slowest relaxation process, at which point the net velocity is suppressed by more than 13 orders of magnitude. To compute late times to 1e-10 accuracy is a waste of time and generally limited by floating point precision.

To reduce this waste, we aim for adaptive Simpsons. Essentially, we evaluate a 1-4-1 triplet and then consider doubling the timestep. It turns out that RK4 is limited to timesteps of $dt = 1/(2\,|\max(M)\,|)$ and this is typically so fast converging that another factor 1/10 is enough to get essentially no errors – but we waste a lot of time at late times. To reduce this, we skip intermediate steps by using $R_{2dt} = R_{dt}^2$ because $u_{n+1} = Ru_n$ can be repeated. By squaring the matrix repeatedly we can exponentially increase the effective timestep and soon skip 99% of the time steps.

We use an error estimate to determine when the time step should be increased. Following standard practise, we compare at a given moment in time the contribution of 2 steps with dt and a single step 2dt to estimate the error. If the *relative* error made is less than a user-defined accuracy (e.g. 1e-10) then we double the timestep. Overall, this leads to an integration error close to the user specified accuracy.

Advice

For any future implementers of similar strategies, we include a word of advice. It is clear that ultimately the limits of this algorithm as a whole lie in the size of n. With increasing n, the matrix becomes increasingly sparse. We ultimately end up using the central diagonal, 4 diagonals to either side and 8 terms on each row interacting between the sheets. If $n = 512$ (matrix size 1024), this gives rise to 17 out of 1024 elements non-zero. That 17 does not change with n and is highly inefficient. Although the zeros are used when we double time steps using R^2, the time it takes to compute R^2 becomes increasingly painful as n increases and is now at the limit where it takes more time than it saves from skipped t steps even after many times taking the square. I cannot give you a recipe, but this is where I suspect any further algorithmic changes will save time. Either from sparse matrices (but then you go back to many wasted time steps at late times) or from changing something more fundamental.

k_a-integral

The final integral is k_a. We here use Simpsons rule with the special clause that the points evaluated must be in the u state to be able to initialise a proper $\delta(k_a{}' - k_a)$ at time 0. This is a minimal requirement. Typically, we use 30 points for k_a and as many as time will allow for k_a' (i.e. *u*). It turns out that n (number of k_a') must be a multiple of fs_points (number of k_a) for this to work without any extra errors.

Error estimates

If there is one aspect we do not compromise on, that must be error estimates and tests. Science is not the same as business in that sense. Correctness is everything.

The way errors are here estimated is to compute σ at every magnetic field 6 times using a standard technique. Once for the value, once with half n, once with half fs_points, once with half the cutoff time on the t integral, once with a double error cutoff (accuracy) requirement for dt doubling, and once with a twice larger initial dt. We take the maximum difference found as the error estimate. Note that the last 3 are essentially never leading and the total cost of the whole thing is about 5x a calculation of σ without error estimates. However, by scanning all settings this way we ensure that the numerical error is captured well. Note that for Simpson integrals, the error usually is overestimated by a factor 3 because of the rate of convergence.

We progress the errors in σ into errors on ρ using standard error propagation. Essentially, we treat the above errors as Gaussian standard deviations (which overestimates them further). Let the resistivity be given as follows:

$$\rho_{ij} = f(\sigma_1, \sigma_2, \sigma_3)$$

Then we propagate the error by evaluating the variance in ρ_{ij} from the variance in σ_i. More precisely, let $\delta\sigma_i$ be the described error estimate, then:

$$\delta\rho_{ij}^2 = \left(\frac{\partial f}{\partial \sigma_1}\delta\sigma_1\right)^2 + \left(\frac{\partial f}{\partial \sigma_2}\delta\sigma_2\right)^2 + \left(\frac{\partial f}{\partial \sigma_3}\delta\sigma_3\right)^2$$

These errors are used to create error bars in the plots. Not only are these errors rounded up at every stage, most of the error is not field dependent and plots of the MR from quick and imprecise calculations have been seen to manifest a real error up to 3 orders of magnitude smaller mostly from this fact alone. We aim for errors 10x smaller than the MR size.

On testing in general

This is an opinion section. Testing is incredibly important and significantly neglected across science, but physics in particular. Ask almost any company or programmer by profession and they will be surprised if they never heard of that situation before. So let us spend a few words on why we do this here.

Tests are our principle means to ensure no systemic errors enter the code. This can arise from a simple mistake in the integration weights to severe mistakes in the algorithm – such as making $\widehat{M}$ have rows add to 0 instead of columns as in an early version of the present model. Subtle errors can be avoided with small and quick tests that mostly take time to write and save a wealth of time down to road to identify and fix. Major errors such as the one described are only found because of rigorous high level tests against Drude/RTA theory.

There are test suites with the code for both RTA and beyond-RTA models. These test all sorts of small-scale functionality against expected results. You can take a look in the associated files. Please argue, please maintain a healthy scepticism. We note, without any excuse for mistakes and only to point out how much we value these tests, that this was done during a review process for Science, which puts a lot of time pressure on this work. The reason to do it anyways, is that the aim is not to get results fast, but to get to *the* result fast – and we believe in the process overall we save time by spending time writing tests.

Tests

For the first test, note that isotropic τ is the default, where we take $P(k) = l_b/< v_b >$ as k-independent (whether $< v >$ or $< 1/v >$ is taken barely matters when v varies by 1 %). This case shows positive MR and is the central estimate in the paper, bs_type=2. But these are hard to compare to RTA because they include separate small- and back-scattering processes that behave slightly differently even when their characteristic time is equal.

To test against the RTA, we implement bs_type=5 mode, which has no interaction between neighbours, but simply exponential decay with isotropic τ to mimic the RTA. As mentioned before, $u(t, k'_a) = \delta(k_a - k'_a)e^{-t/\tau}$. The results should match the RTA results (albeit computationally a lot more expensive). To make these tests as accurate as possible, we operate on an artificial Fermi surface with high anisotropy $\frac{\rho_{aa}}{\rho_{bb}} = 1.4$ that just remains quasi-1D.

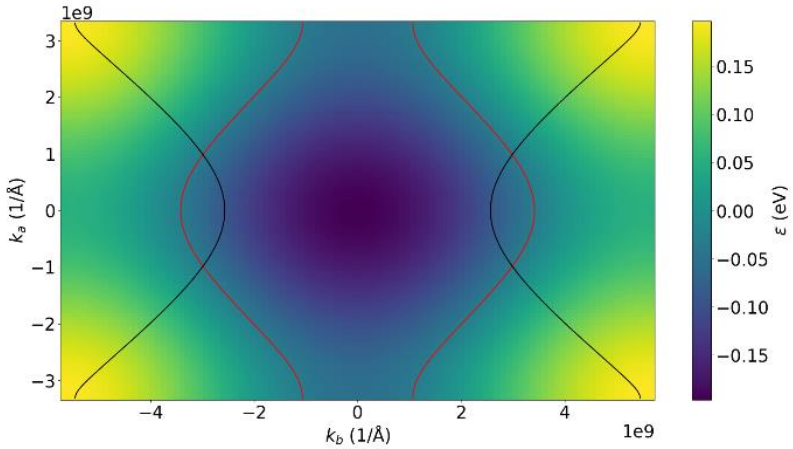

The highly anisotropic Fermi surface. The black sheet has a v_b anisotropy of 5x rather than ~1% for Merino/Nuss.

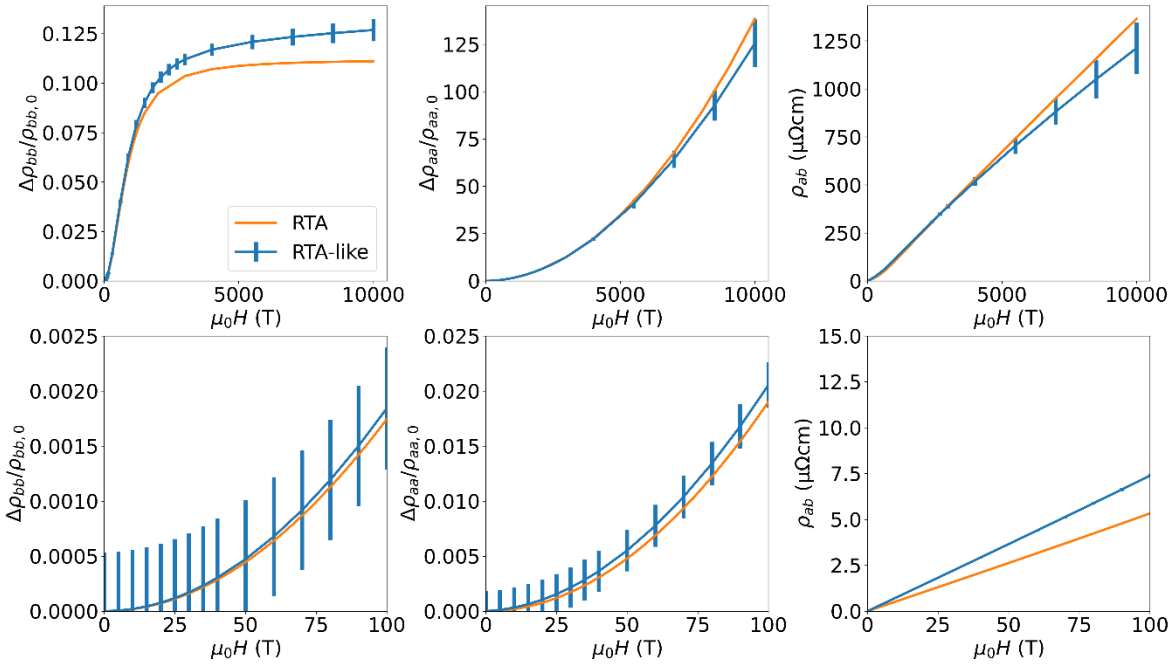

See code '15_show_with_RTA.py' for details. Columns show components, the second row zooms in at low fields. The saturation MR is 0.1, 4 orders of magnitude larger than for the Merino (let alone Nuss) Fermi surfaces, yet still less than the experimental results at lowest temperatures, despite being close to the Lifshitz transition to form a 2D Fermi surface. The main reason for a slight divergence at highest fields we suspect is broadening under cyclotron motion even in the absence of scattering. The errors are nevertheless limited and it may be observed that the results are accurate at low fields in the second row.

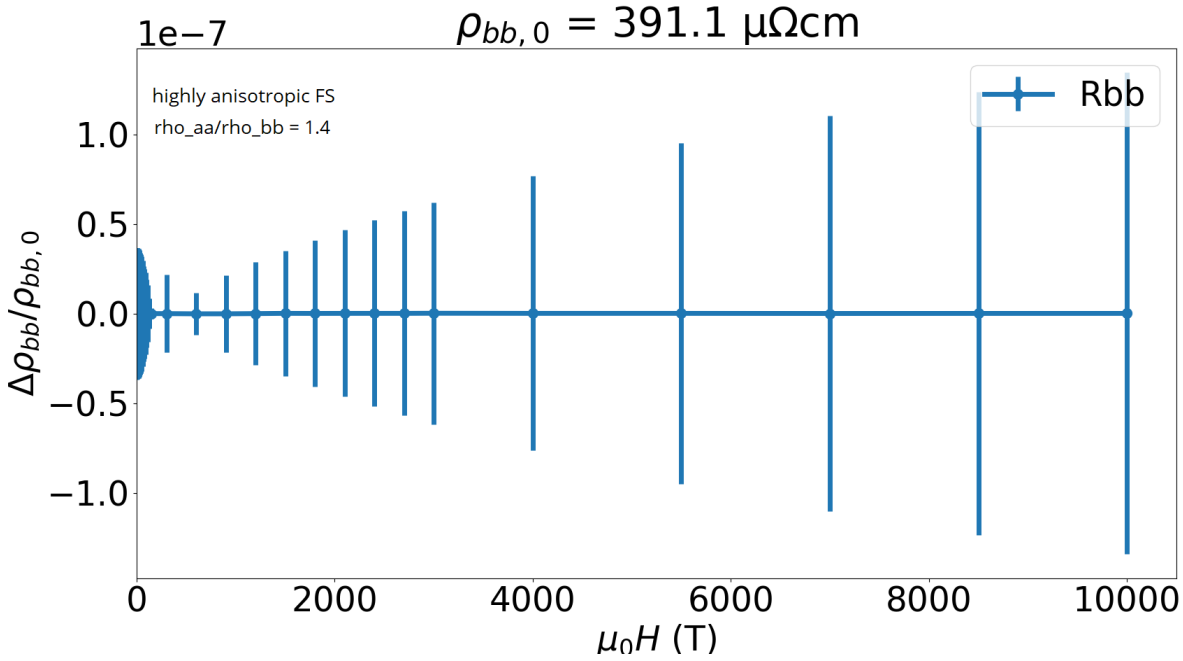

The second test revolves around an insight. Although our central results are based on isotropic-P models, this is *not* the most realistic. We recall that the idea of backscattering was based upon impurities and excitons located in real space. For such scattering mechanisms, isotropic l_b is more likely. With the option bs_type=2, we implement $P(k) = l/v_b(k)$ where l is taken to be 1 nm. We still do calculations with the highly anisotropic Fermi surface where $\frac{\rho_{aa}}{\rho_{bb}} = 1.4$. Perhaps surprisingly, this still leads to exactly zero MR as shown in the figure below. To show this is not an aberration, we present in the next section an analytical proof that within RTA isotropic l_b indeed gives rise to zero *b*-axis MR. These numerical results therefore merely confirm this situation persists beyond the RTA.

Note that other forms of Umklapp scattering, especially isotropic end states, can be attempted with the code (bs_type=4). We have not found any indication of significantly different MR.

7) Analytical proof zero MR

We here consider the case of isotropic l_b in the relaxation time approximation. The aim is to show that this case manifests zero *b*-axis MR.

We will only show this assuming it accepted that σ_{bb} is monotonic with magnetic field, which indeed is satisfied within every calculation within our knowledge. Then we aim to show that with isotropic l zero MR follows by comparing the zero-field and infinite-field conductivity. Note that $\lim_{B\to\infty}\sigma_{bb}$ vanishes in any dimension above 1, but remains finite in 1D. By definition

$$\frac{\lim_{B\to\infty}\rho_{bb}}{\rho_{bb}(0)}=\lim_{B\to\infty}\frac{\sigma_{aa}(\sigma_{aa}(0)\sigma_{bb}(0)+\sigma_{ab}(0)^2)}{(\sigma_{aa}\sigma_{bb}+\sigma_{ab}^2)\sigma_{aa}(0)}$$

Of course, $\sigma_{ab}(0)$ vanishes following symmetry considerations without time reversal symmetry breaking by a magnetic field.

$$\frac{\lim_{B\to\infty}\rho_{bb}}{\rho_{bb}(0)}=\lim_{B\to\infty}\frac{\sigma_{aa}\sigma_{bb}(0)}{(\sigma_{aa}\sigma_{bb}+\sigma_{ab}^2)}$$

$$\sigma_{ij}=\frac{e^2}{4\pi^3}\int_{FS}d^2k\frac{v_i}{\hbar v_F}\int_0^\infty dt\ v_j(-t)e^{-\frac{t}{\tau}}$$

Take the limit to high field. Physically, this means the Fermi surface is traversed with almost no decay and the inner integral becomes $< v_j >$. $< x >$ denotes a Fermi *sheet* average, i.e. $\int_{sheet}dkx\ /\ \int_{sheet}dk$. This immediately results in $< v_a >= 0$, but $< v_b > \neq 0$ in quasi-1D with H//c. The establishes σ_{aa} and σ_{ab} both vanish. We remain with:

$$\frac{\lim_{B\to\infty}\rho_{bb}}{\rho_{bb}(0)}=\lim_{B\to\infty}\frac{\sigma_{bb}(0)}{\sigma_{bb}}$$

Without magnetic field, σ_{bb} is quickly shown to be given by the average mean free path. The inner integral simplifies because v and τ are time-independent given the lack of cyclotron motion.

$$\sigma_{bb}(0)=\frac{e^2}{2\pi^2\hbar c}\int_{-\pi/a}^{\pi/a}dk_a\int_0^\infty dt\ e^{-\frac{t}{\tau}}v_b(0)=\frac{e^2}{2\pi^2\hbar c}\int_{-\pi/a}^{\pi/a}dk_a\,\tau v_b=\frac{e^2}{\pi\hbar ac}<l_b>$$

The other conductivities must be evaluated in the $B\to\infty$ limit for which we need only the leading order. In this limit, the quasi-particle can traverse many sheets. We can simplify this by introducing a sheet traversal time, without approximation:

$$\lim_{B\to\infty}\sigma_{bb}=\frac{e^2}{2\pi^2\hbar c}\int_{-\frac{\pi}{a}}^{\frac{\pi}{a}}dk_a\frac{1}{1-P}\int_0^{t_{sheet}}dtv_be^{-t/\tau}$$

Here, the middle term expresses the number of Fermi sheets traversed through the probability P to survive 1 sheet. The final term has in leading order no decay within a single sheet. Use $\dot{k}=qv_FB/\hbar$ since $v\perp B_c$:

$$P=1-\int_{FS}dk\frac{\hbar}{\tau qvB}e^{-\frac{(k_a-k_{a0})\hbar}{qvB\tau}}=1-\frac{\hbar}{qB}\int_{FS}dk\frac{1}{l_b}\frac{l_b}{l}+O(l^2)=1-\frac{\hbar}{qBl_b}\int_{FS}dk\frac{v_b}{v_F}+O(l^2)$$

$$\int_0^{t_{sheet}}dtv_be^{-t/\tau}=\frac{\hbar}{qB}\int_{FS}dk\frac{v_b}{v_F}+O\left(t_{sheet}<\frac{1}{\tau}>\right)$$

In the high field limit only the first term here is relevant. The two integrals over v_b/v_F cancel and we are left with:

$$\lim_{B\to\infty} \sigma_{bb} \approx \frac{e^2}{2\pi^2\hbar c} \int_{-\frac{\pi}{a}}^{\frac{\pi}{a}} dk_a \; l_b = \frac{e^2 l_b}{\pi\hbar c a}$$

We can now observe that $\lim_{B\to\infty} \sigma_{bb} = \sigma_{bb}(0)$ in the isotropic-l_b limit. Within the unproven conjecture that the conductivity is indeed monotonic, this proves also that there is zero MR.

8) MR saturation

The MR saturation is a second key argument why Boltzmann theory falls short of explaining the LMO MR. We note that $\Delta\rho_{bb}/\rho_{bb}$ is about 5e-5 at 1 T at room temperature.

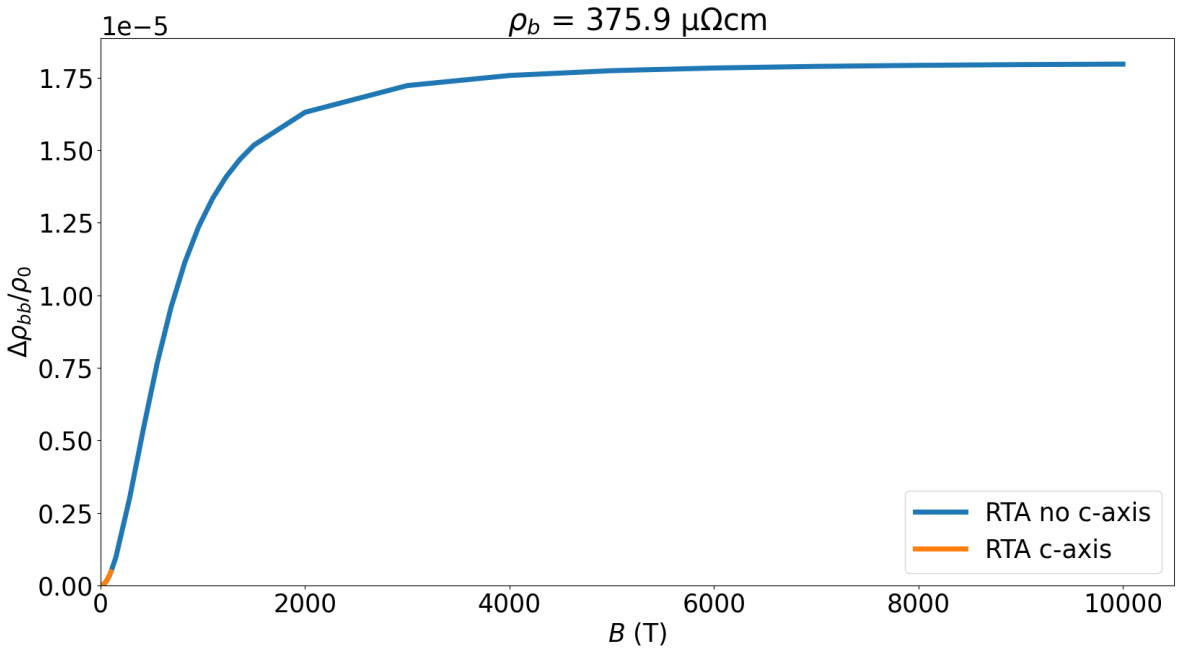

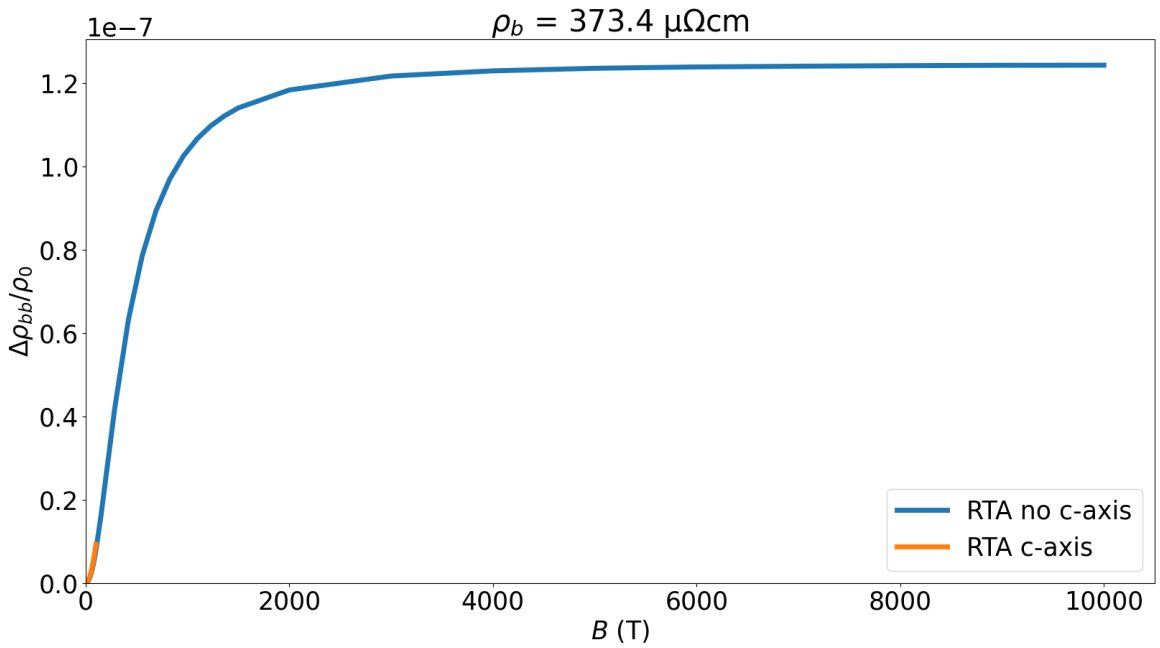

The above shows the Merino (first) and Nuss (second) Fermi surface. The saturation MR is entirely geometrical, use 'c_axis_vizualise_results.py' to obtain these graphs. It can be seen that in both cases the saturation MR is lower than the MR in experiment even at 1 T and 300 K. Such a marked violation of the saturation MR cannot be fixed with simple scattering rate mechanisms for they wash out at high fields.

Instead, either hot spots or strong Fermi surface anisotropy must be present. However, we have shown above already that a nearly-2D variant gives rise to *b*-axis MR saturation at a level of 0.1. This requires anisotropy such that $\frac{\rho_{aa}}{\rho_{bb}} = 1.4$ rather than 80 at 300 K and 150 at 5 K [1]. Even in this extreme case, the experimental *b*-axis MR reaches 0.6 at 5 K and 8 T without signs of saturation.

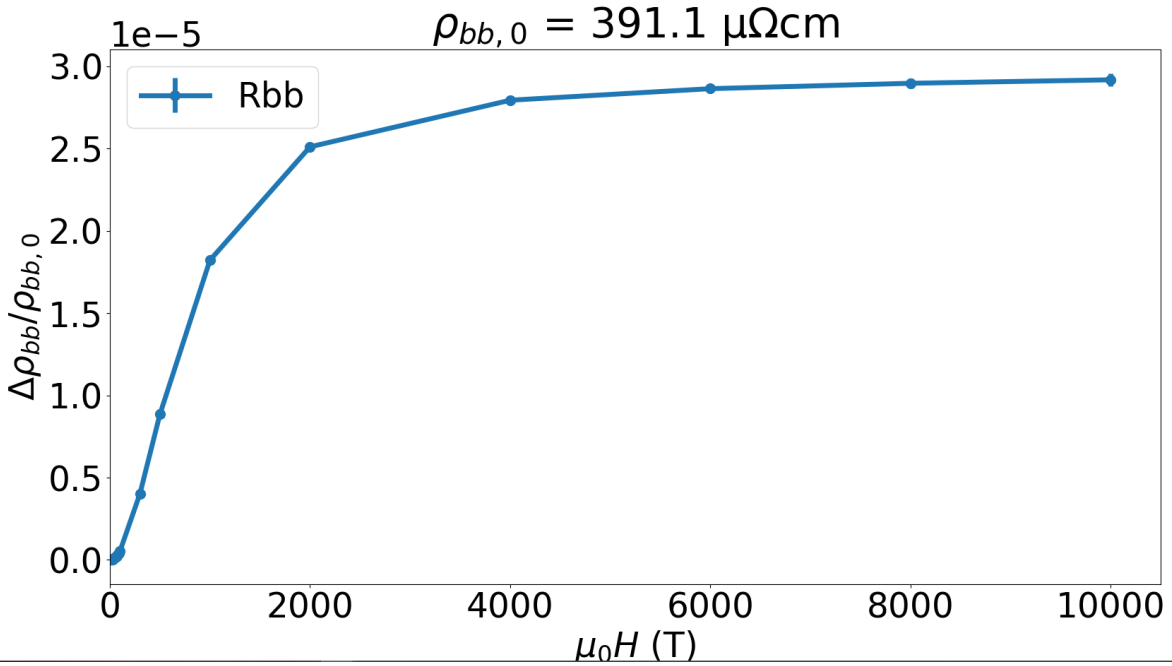

These are the high field results on the Merino Fermi surface. Note that the results above suggest the saturation MR may be overestimated. Regardless, the saturation MR is largely unaffected by moving from RTA to SAS because scattering washes out at high field. (Made with '04_show.py' on file 73)

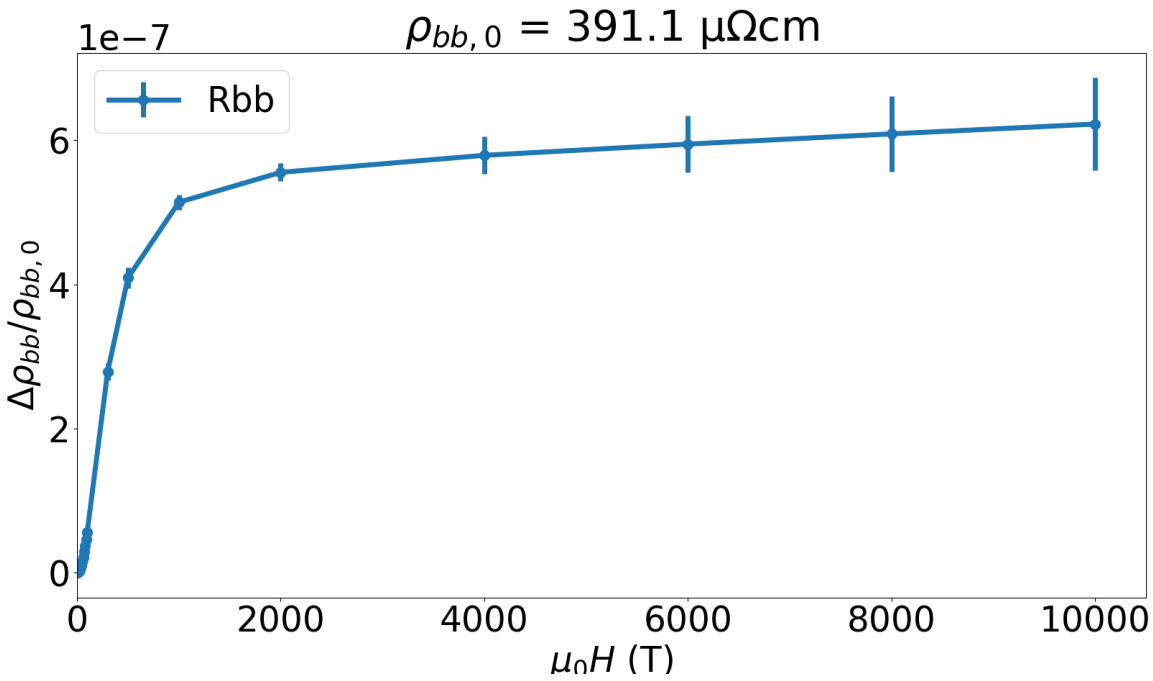

The same for the Nuss Fermi surface (file 74).

Bibliography

[1] Mercure, J.-F. *et al.*, Phys. Rev. Lett. 108,187003 (2012)

[2] N. E. Hussey *et al.* Phys. Rev. Lett. 89, 086601 (2002)

[3] "The influence of small angle scattering on metallic conduction" by Pippard 1968 Proc Roy Soc A 305 291-318